Chapter VII

ANALYSIS OF VARIATIONS IN AMPLITUDES AND
TRAVELTIMES WITH OFFSET AND MIDPOINT

Lateral variations in rock properties cause complex variations of amplitudes and traveltimes with offset on common-midpoint gathers. A theory for the interpretation and inversion of these complex variations is presented. The application of the theory to seismic data from a producing gas field shows correlations of interpreted velocity and amplitude anomalies with diffractions observed on common-offset sections.

Conventional processing of high quality seismic data involves a high degree of data reduction. The stacking process implies assumptions about the conditions where the data was collected, such as the absence of rapid lateral variations in velocity or absorption. A great deal of information will be lost in stacking when such variations are present, especially if the signal-to-noise ratio is good on the unstacked data. In this report examples of such data are presented along with methods for their inversion.

The dataset used is a seismic line across the Grand Isle gas field off the shore of Louisiana. The data was made available to the Stanford Exploration Project by Dr. Ralph Shuey of Gulf Science and Technology Company in Pittsburgh. Recording parameters for the line are listed in table 7.1. Typical common-midpoint gathers are shown in figures 7.1-7.5, and a common-offset section of the fifth offset is shown in figure 7.6. These plots show a number of interesting features. One of the most striking is the rapid and seemingly irregular changes in the amplitude of the bright spot reflection at 2.3 seconds, with offset.

110

TABLE 7.1. SHOOTING GEOMETRY

(all dimensions in feet)

Energy source	Airgun
Source depth	30
Shot interval	82
Group interval	164
Near geophone	743
Far geophone	8498
Cable length	7756
Fold	48
Filter	5-144 Hz

These amplitude variations are much too strong to be explained by the angle-dependence of the reflection coefficient, or the destructive and constructive interference between closely spaced reflectors. Many of the amplitude anomalies shown in figure 7.6 correlate for several reflectors: for example, the amplitude variations around midpoint 287 appear to be present on all visible reflectors from about 1.5 seconds down to the bottom of the section. This points towards transmission effects in the overlying rocks as the most plausible explanation. In order to investigate this further, the power in each trace for the interval from 1.5 to 3 seconds was integrated for each midpoint, and for all the offsets. After this was done, it became apparent that some of the offsets had systematically higher or lower amplitudes than the others. In order to remove this effect, each offset was normalized by dividing by the median power for that particular offset. The logarithm of this result is plotted in figure 7.7, as normalized amplitude versus midpoint and offset.

High amplitudes show up dark on the plot; amplitude variations caused by variable reflectivity along the reflectors should show as vertical rectangles on the plot, while variations caused by shot amplitudes should have a 45-degree slope. The black streak on the left side of the plot is caused by two shot locations with no data - the tapes containing garbage. Close inspection reveals a large number of small amplitude fluctuations that are parallel to the streak caused by the bad data; these are undoubtedly caused by variations in the shot amplitude.
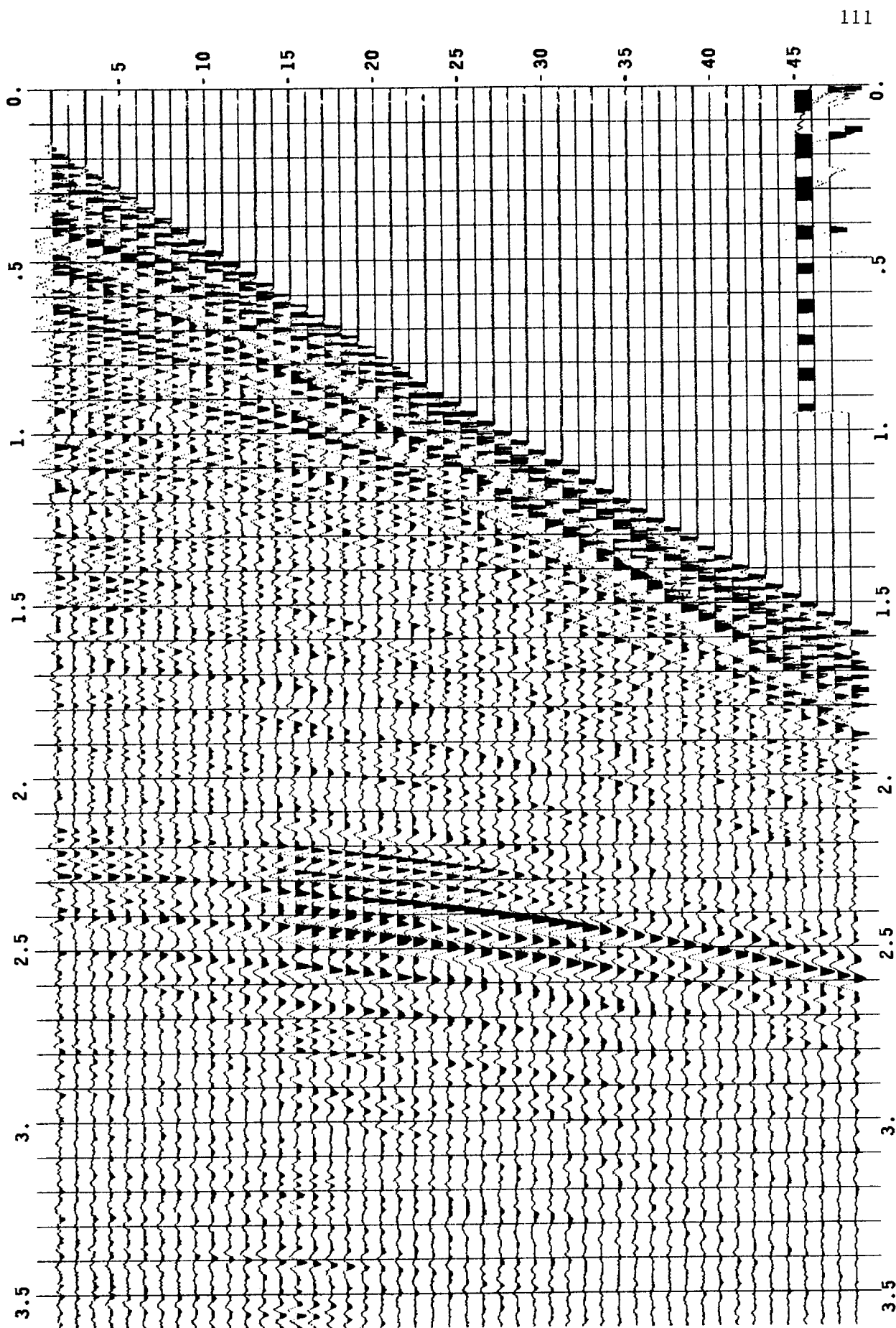
FIG. 7.1. Common-midpoint gather 210. No processing has been applied to the data, except for a display gain proportional to time. Recording parameters are given in table 7.1.
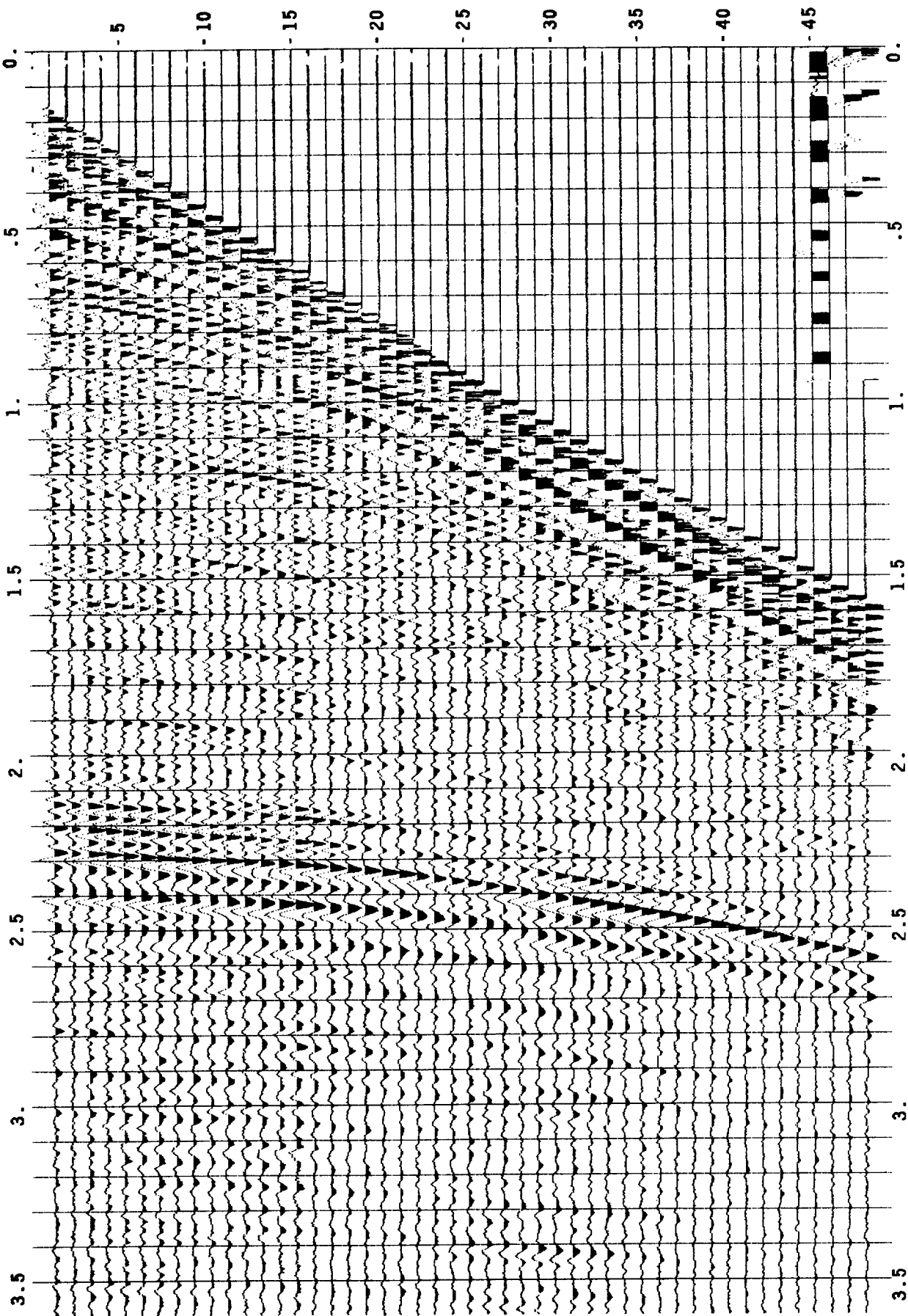
FIG. 7.2. Common-midpoint gather 220. The reflection at 2.3 seconds shows deviations from hyperbolic moveout.
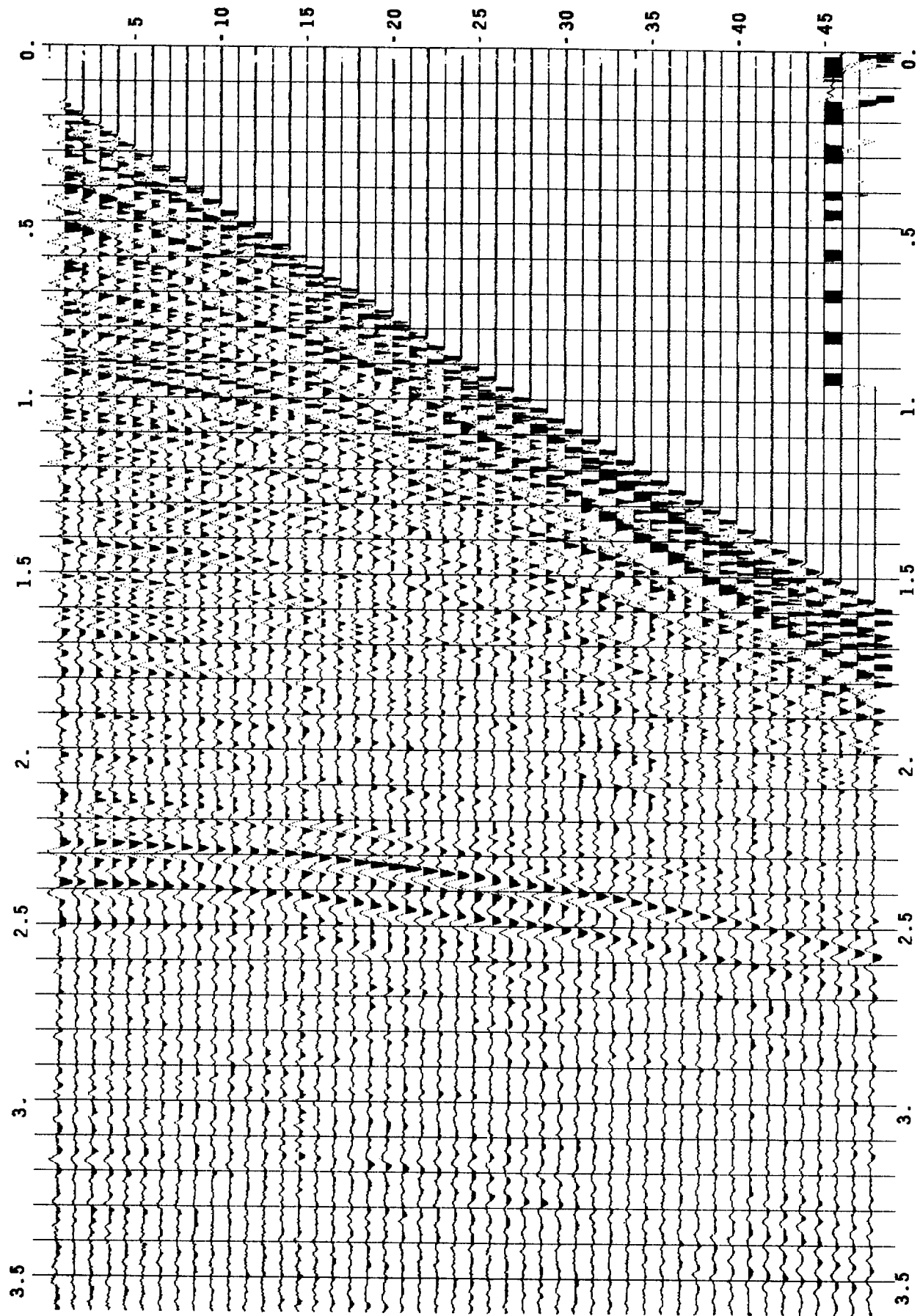
113

FIG. 7.3. Common-midpoint gather 230. The distance separating figures 7.1 and 7.2, and figures 7.2 and 7.3, and figures 7.4 and 7.5 is 250 meters (820 feet).
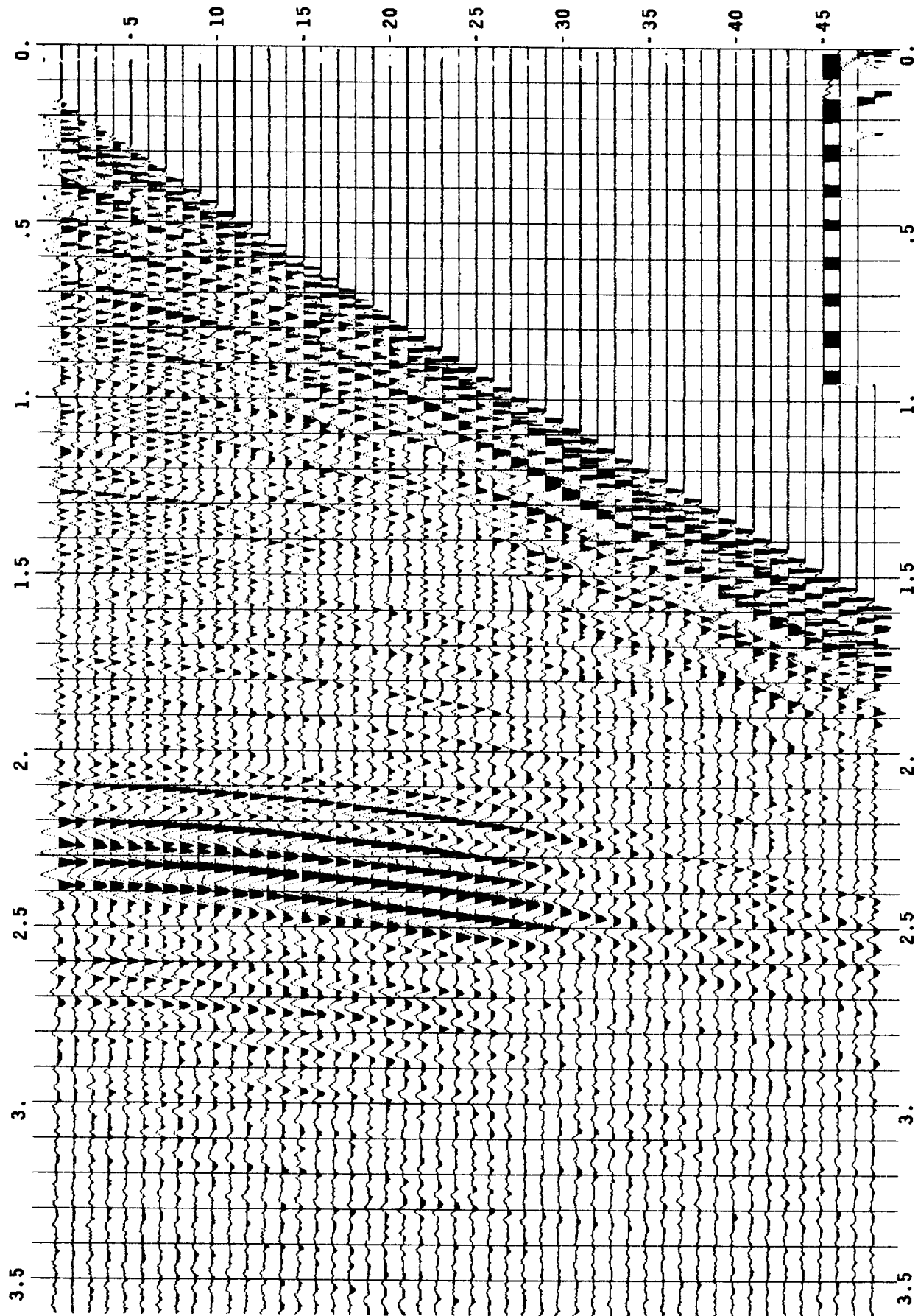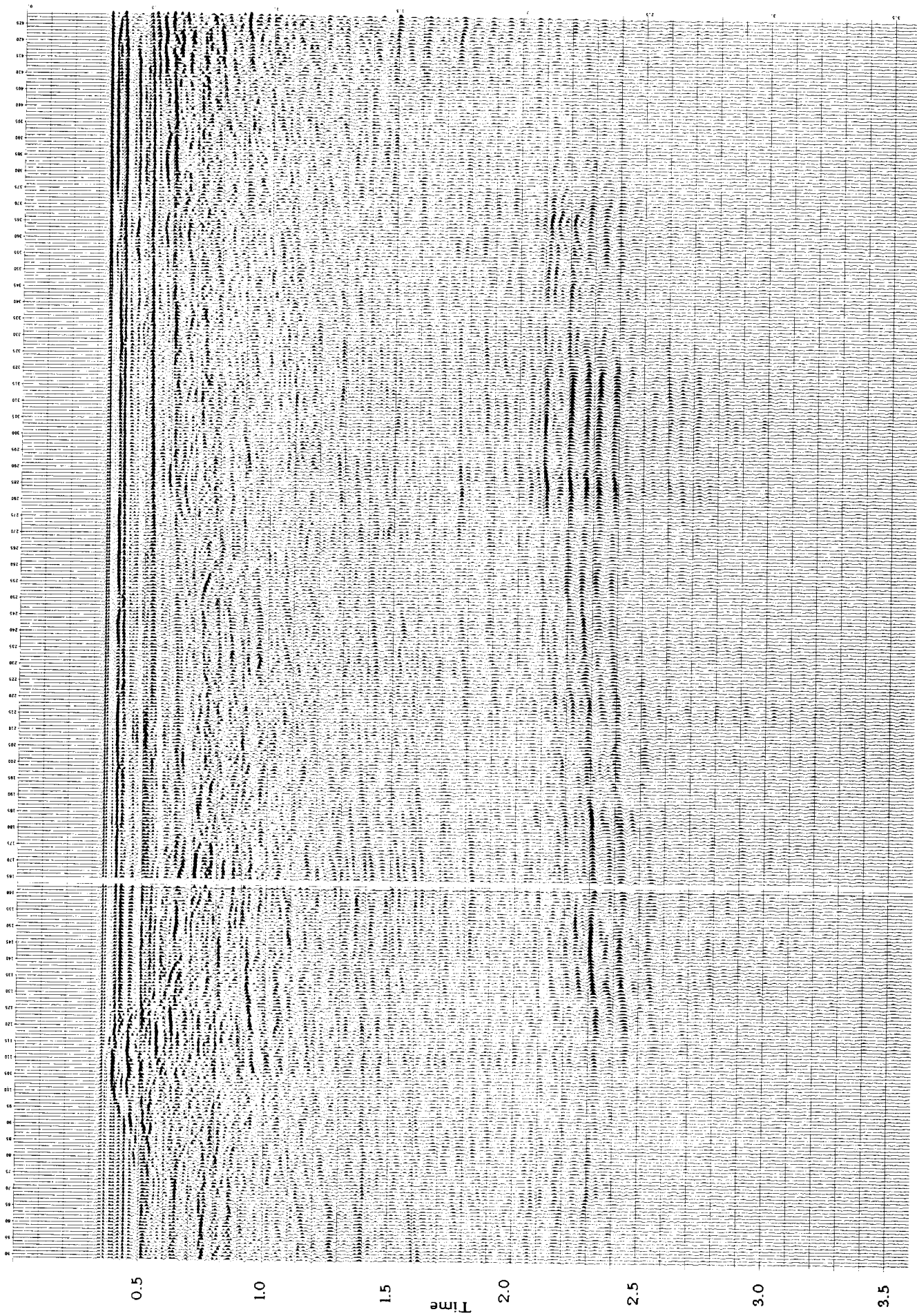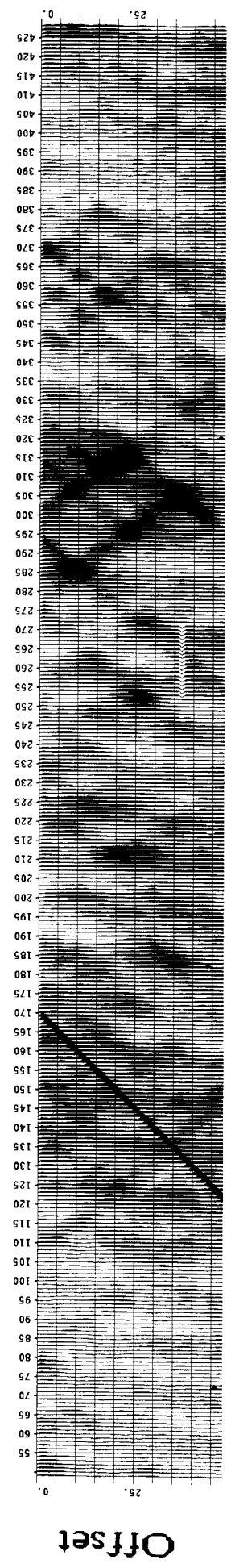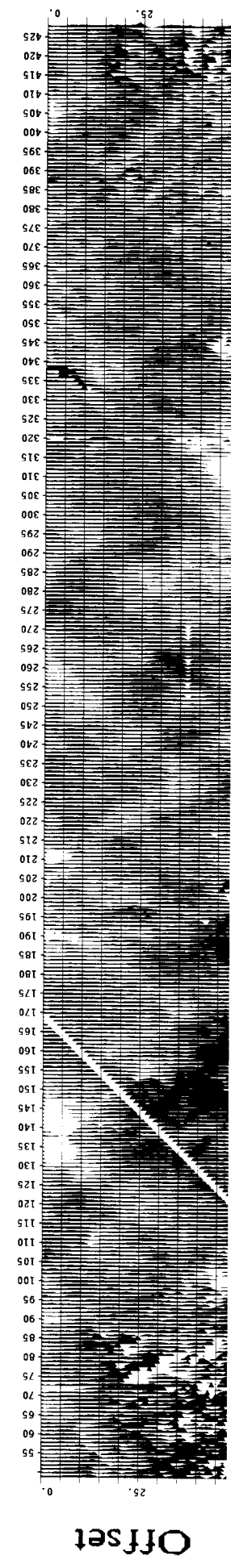
FIG. 7.5. Common-midpoint gather 315.

FIG. 6.

Offset

FIG. 7.

Offset

FIG. 9.

Depth

FIG. 15.

Depth

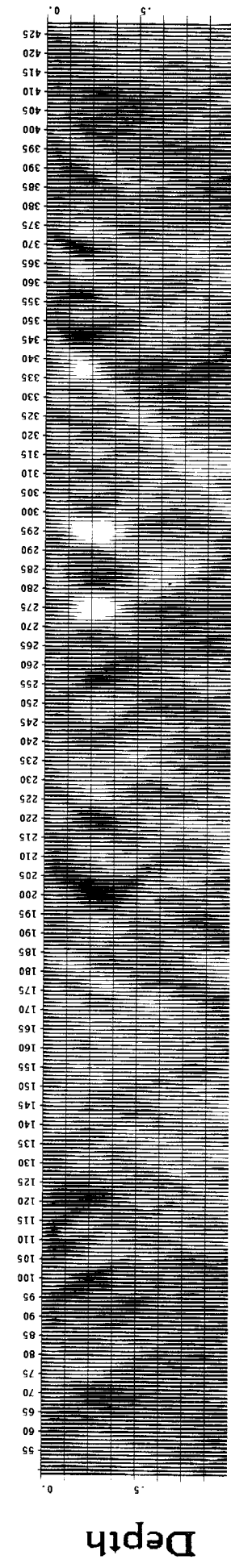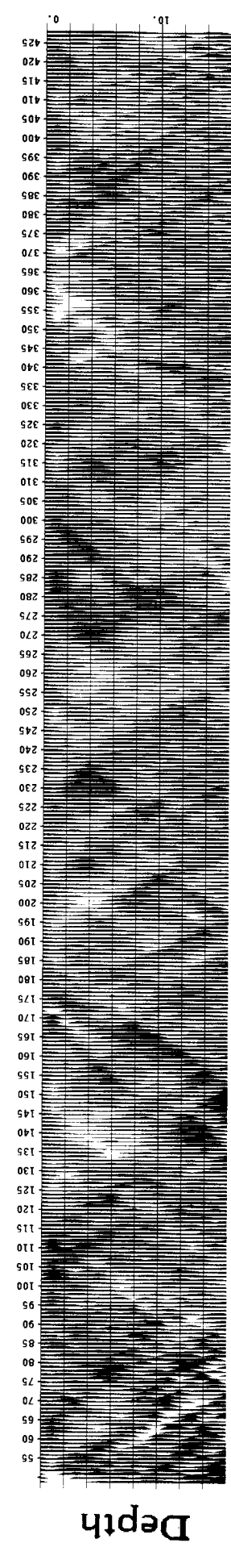FIG. 16.

118

FIG. 7.6. A common-offset section for the fifth offset. Shot receiver distance is 320 meters (1070 feet) and trace spacing is 25 meters (82 feet). The amplitude pattern and details of the shape of the bright-spot reflector change from offset to offset. Note the good signal-to-noise ratio and the diffraction patterns in the first second of data.

FIG. 7.7. The logarithm of the power is plotted versus midpoint and offset. The power was integrated over a window that extended after NMO from 1.5 to 3 seconds. Systematic offset dependence was removed by dividing the power at each offset by the median power for that offset.

FIG. 7.9. Traveltime anomalies are shown versus midpoint and offset. The times shown were obtained by crosscorrelation with a sum trace, after time shifts applied as in figure 7.8. The window length was 1.024 seconds. Black indicates delays.

FIG. 7.15. Result of applying the iterative-median inversion to the amplitude data plotted in figure 7.7. The depth scale is relative to the depth of the bright spot which is approximately 8000 feet. The interval from the bright spot to the surface was divided into 16 layers. Black on this plot indicates low amplitudes (high absorption).

FIG. 7.16. Black indicates low velocities. The result of applying the iterative-median inversion to the amplitude data. Slowness is displayed in the same manner as the absorption in figure 7.15.

One potential explanation for the amplitude variations, as they are observed on individual midpoint gathers, is that they are caused by variations in shot strength or by variations of the properties of the sea bottom. Inspection of figure 7.7 shows that this does not suffice to explain some of the larger features visible on the plot. The large amplitudes (dark on the plot) occur in bands that have significantly steeper slope than the shot effects. There is also a bimodal distribution of slopes, since bands that go either left or right with offset occur with about the same frequency.

A closer look at figures 7.1-7.5 shows in addition to the amplitude effects, deviations from hyperbolic moveout. Figure 7.8 shows the gather from figure 7.2, after a time-independent time shift was applied to the traces, as appropriate for an NMO of an event at 2.3 seconds with an RMS velocity of 7000 feet/second. The plot shows deviations in traveltime of almost 20 ms, even though there is excellent match at the far and near offsets. Figure 7.9 shows a plot of time shifts, as determined by crosscorrelations with the sumtrace for each gather, for all the shots and all the offsets, using a one-second time window. This plot shows the same qualitative features as in figure 7.7, but there is a great deal more noise, some of which is probably caused by cycle jumps in the crosscorrelation.

Theory

A theoretical framework for the interpretation of midpoint-offset anomalies of the type we have shown will be presented. Our earth model is shown in figure 7.10. We assume that our observations may be related to some quantity $d(h,y)$ that is the line integral along the raypath of some rock parameter $w(z,y)$. Earth model assumed. The value of the vertical coordinate, z, is zero at the reflector and z_o at the surface.
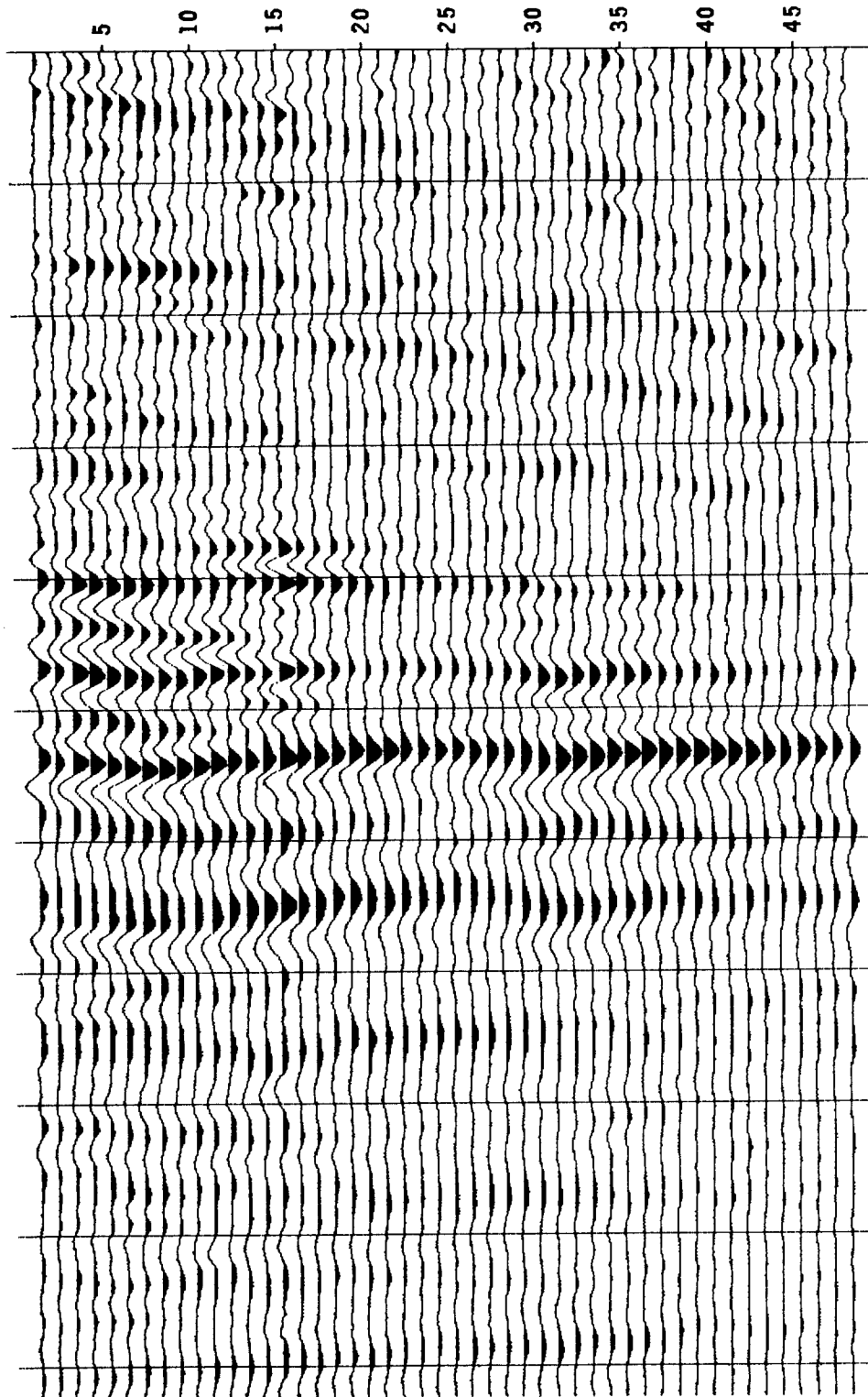
FIG. 7.8. Midpoint gather 220 (same as in figure 7.2) after moveout. Shown is one second window centered at 2.3 seconds, time shifted according to an NMO for an event at 2.3 seconds, using a velocity of 7000 feet/s.
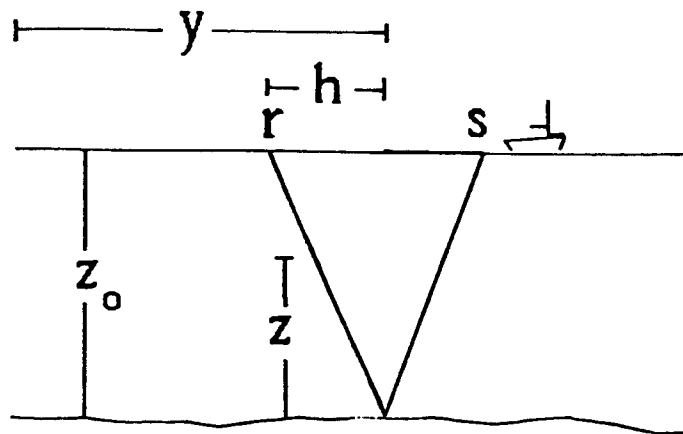
FIG. 7.10. Earth model assumed. The value of the vertical coordinate, z, is zero at the reflector and z_0 at the surface.

For example, the traveltime is the integral of the slowness $1/v$:

$$t = \int \frac{ds}{v(z,y)} \qquad (7.2)$$

Another example is the amplitude decay of a monochromatic wave due to absorption:

$$A = \exp\left[-\int \alpha(z,y)ds\right] \qquad (7.2)$$

where A is the amplitude and α is related to the intrinsic quality factor Q by

$$\alpha = \frac{\pi f}{Qv(f)} \qquad (7.3)$$

where f is frequency. The dispersion that is a consequence of causality has the effect of making the velocity v slightly dependent on frequency.

For a broad-band source in a medium where Q is independent of frequency, the width of a pulse τ is given by

$$\tau = c \int \frac{ds}{Q(z,y)v(z,y)} \qquad (7.4)$$

where c is a constant that depends on the particular measure of pulse width used [Kjartansson, 1979]. These three different types of observations may be treated with the same tools if refractions caused by lateral variations in velocity are neglected. The effects of velocity variations with depth may be accounted for by the application of a coordinate transformation. For velocity variations of a few percent or less, the effect of ray bending on the total path length is small. The assumption of lateral variations on the order of a few percent or less appears well-justified for the present dataset.

If it is further assumed that the measurements are appropriate for primary reflections from a single reflector, or a group of closely spaced reflectors with dips small enough to justify the assumption that the reflector point is directly below the midpoint (migration is not necessary), then we may refer to figure 7.10, and write

$$d(h,y) \quad = \quad \int_{0}^{z_0} \frac{(h^2+z_0^2)^{\frac{1}{2}}}{z_0} \left[w(z,y-h\frac{z}{z_0}) + w(z,y+h\frac{z}{z_0}) \right] dz \qquad (7.5)$$

Since the average offset effect has been removed through the normalization and NMO of the data in figures 7.7 and 7.9, we may drop the cosine factor in equation (7.5):

$$d(h,y) \quad = \quad \int_{0}^{z_0} \left[w(z,y-h\frac{z}{z_0}) + w(z,y+h\frac{z}{z_0}) \right] dz \qquad (7.6)$$

If the function $w(z,y)$ is specified, for example, on a discrete grid, equation (7.6) may be used to model the observations. Figure 7.11 shows the result of a forward calculation from the model shown in figure 7.12. Linear interpolation between adjacent y points in each layer was used. The general character of the synthetic is quite similar to that of the data. Equation (7.6) may be Fourier-transformed over the midpoint coordinates; the result is

$$D(h,k_y) \quad = \quad 2 \int_{0}^{z_0} \cos(h\frac{z}{z_0}k_y) \, W(z,k_y)dz \qquad (7.7)$$
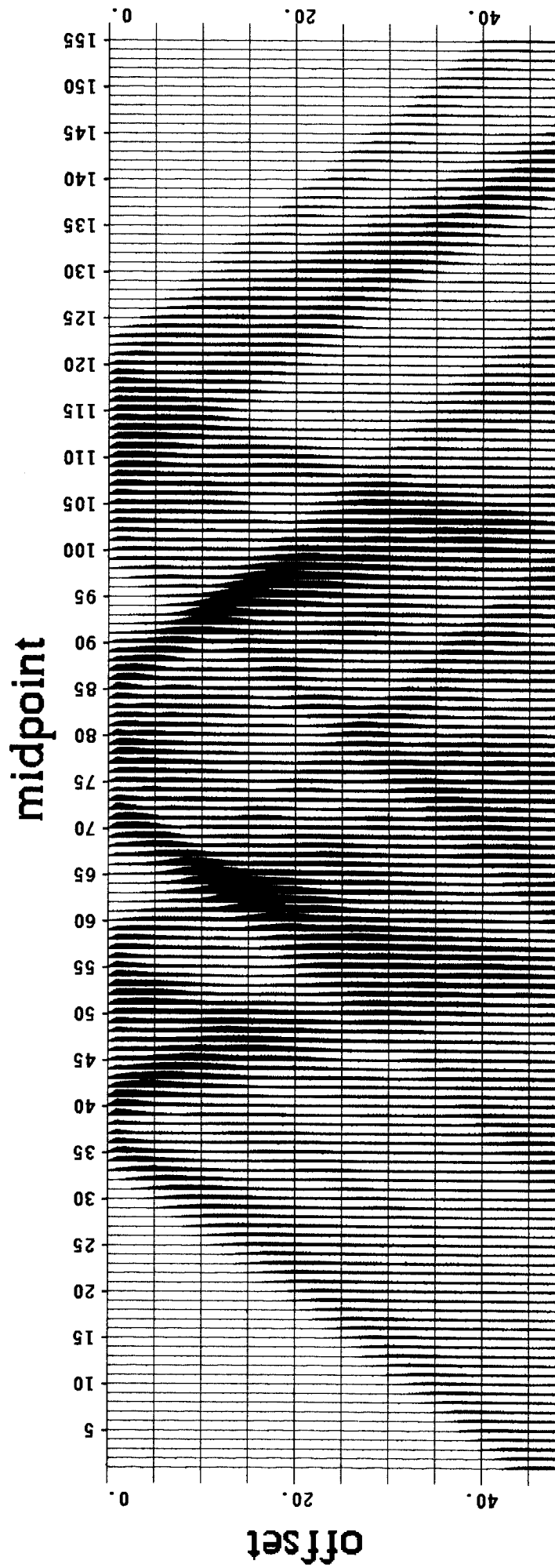
FIG. 7.11. A synthetic midpoint-offset display, computed by evaluating the integral in equation (7.6) numerically, for the structure shown in figure 7.12.
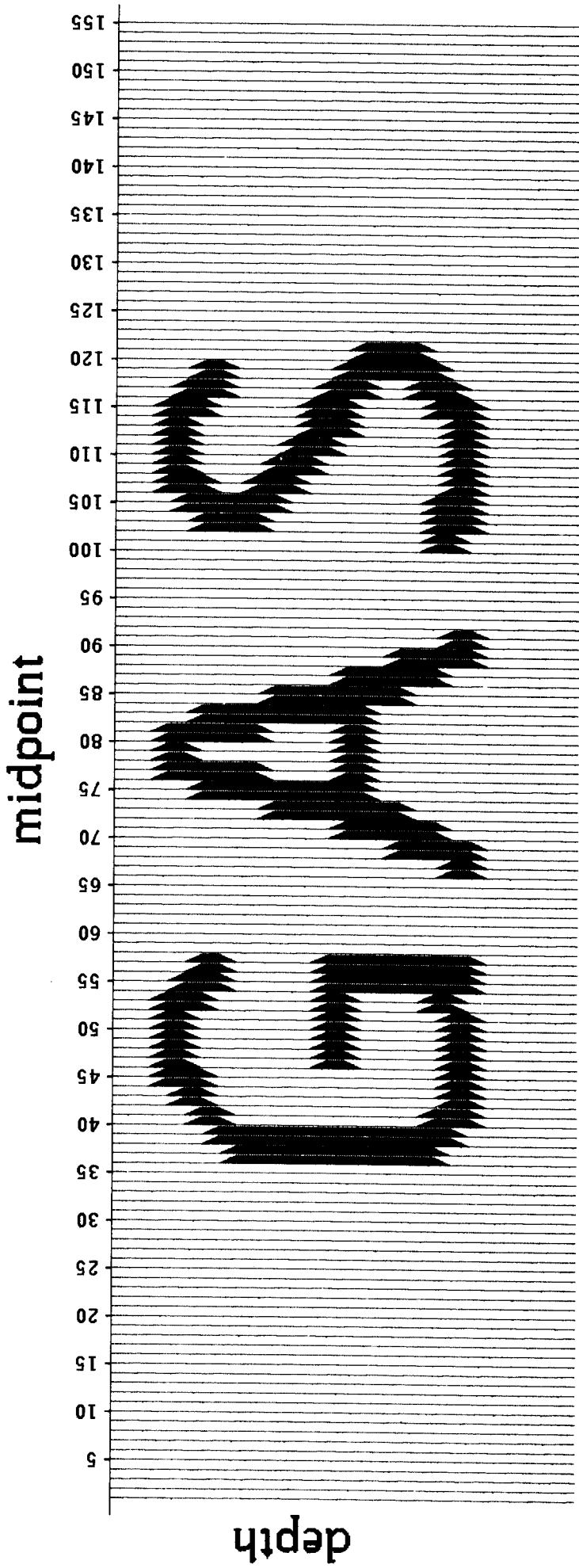
FIG. 7.12. The structure used to compute the synthetic in figure 7.11. The interval from the reflector to the surface is divided into 26 layers.

The form of the integrand in (7.7) is a Fourier transform from the z-domain to the h-domain, except for the integration limits. Thus it is readily seen that the component of the observations which changes most slowly with offset is controlled by the material closest to the reflector, and that the near offsets provide information about the long wavelength components of W, while the far offsets provide the short spatial wavelength information.

Observations at a particular offset h are most sensitive to wavelengths in depth on the order of hk_y/z_0. This implies that measurements do not contain information about velocity layers with tangent of dip less than z_0/h_m. where h_m is the maximum half-offset. The maximum observable dip is similarly limited by the near-offset.

Equation (7.7) may be solved numerically if the interval from the reflector to the surface is divided into n_z layers and the integral replaced by a sum. The result is a set of simultaneous equations of the form

$$\bar{d} = \bar{\bar{A}}\bar{w} \tag{7.8}$$

where $\bar{d}$ is a vector of n_h observations for a particular k_y, and $\bar{w}$ is a vector of n_z values of the function $W(z,k_y)$. The $\bar{\bar{A}}$ matrix is given by

$$a_{ij} = 2 \, \Delta z \, \cos(\frac{\Delta z}{z_0} \Delta h k_y ij) \tag{7.9}$$

Equation (7.8) may be solved for $\bar{w}$ using standard least-square methods. In the process of implementing the solution we found it necessary to constrain the solution, since the matrix $\bar{\bar{A}}^T\bar{\bar{A}}$ is highly singular for low k_y values for the reasons discussed above, even when n_z is less than n_h. General methods for introducing constraints into the matrix $\bar{\bar{A}}$ are discussed by Claerbout [1976]. We chose to minimize the norm N given by

$$N = \bar{e}^T\bar{e} + \gamma \bar{d}^T\bar{d} \tag{7.10}$$

where

$$\bar{e} = \bar{\bar{A}}\bar{w} - \bar{d} \tag{7.11}$$

and γ is chosen empirically. The norm N is minimized by solving

$$(\bar{\bar{A}}^T\bar{\bar{A}} + \gamma\bar{\bar{I}}) = \bar{\bar{A}}^T\bar{d} \qquad (7.12)$$

Figure 7.13 shows the results from applying the wavenumber domain (WD) inversion to the synthetic in figure 7.11. Comparison with figure 7.12 shows that much of the low-dip information has been lost, while the steeply dipping components of the original model were recovered reasonably well. When the wavenumber-domain inversion was applied to the data from figures 7.7 and 7.9, the output was severely contaminated by the impulse responses of the spikes in the data, some of which were caused by instrument errors or cycle jumps in the crosscorrelations. One possible way to deal with this would be to run the inversion, compute a synthetic from the result, compare the synthetic to the data, and set data where the residual exceeds a selected threshold equal to the computed value, and then repeat the process as often as needed. Convergence should be very rapid.

Another possible solution would be to apply an iterative solution technique to the data in the time domain and, rather than minimizing the sum of the residuals squared or the L_2 norm, minimize the sum of the absolute values, the L_1 norm. The L_1 norm gives much better results than the L_2 norm when dealing with data of uneven quality [Claerbout and Muir, 1973; Claerbout, 1976]. The method that we have chosen may be considered a modification of either the Simultaneous Iterative Reconstruction Technique (SIRT) that has been used in the field of medical tomography [Dines and Lytle, 1979], or the Gauss-Seidel method used by Wiggins, et al. [1976] to determine residual statics corrections. These methods proceed as follows: A model is used to compute a synthetic, which is then subtracted from the data to get the residual error. Then the mean residual for all data that are affected by each model parameter is divided by the number of layers and added to that model point. This procedure is repeated several times. Our modification of this algorithm consists simply of replacing the mean in the second step by a median. This has proved very effective in eliminating the undesired effects of spikes in the data. Figure 7.14 shows the result of applying the median - iterative method (MI) to the synthetic in figure 7.11. The result is similar to the result of the WD inversion shown in figure 7.13, except that some of the artifacts related to
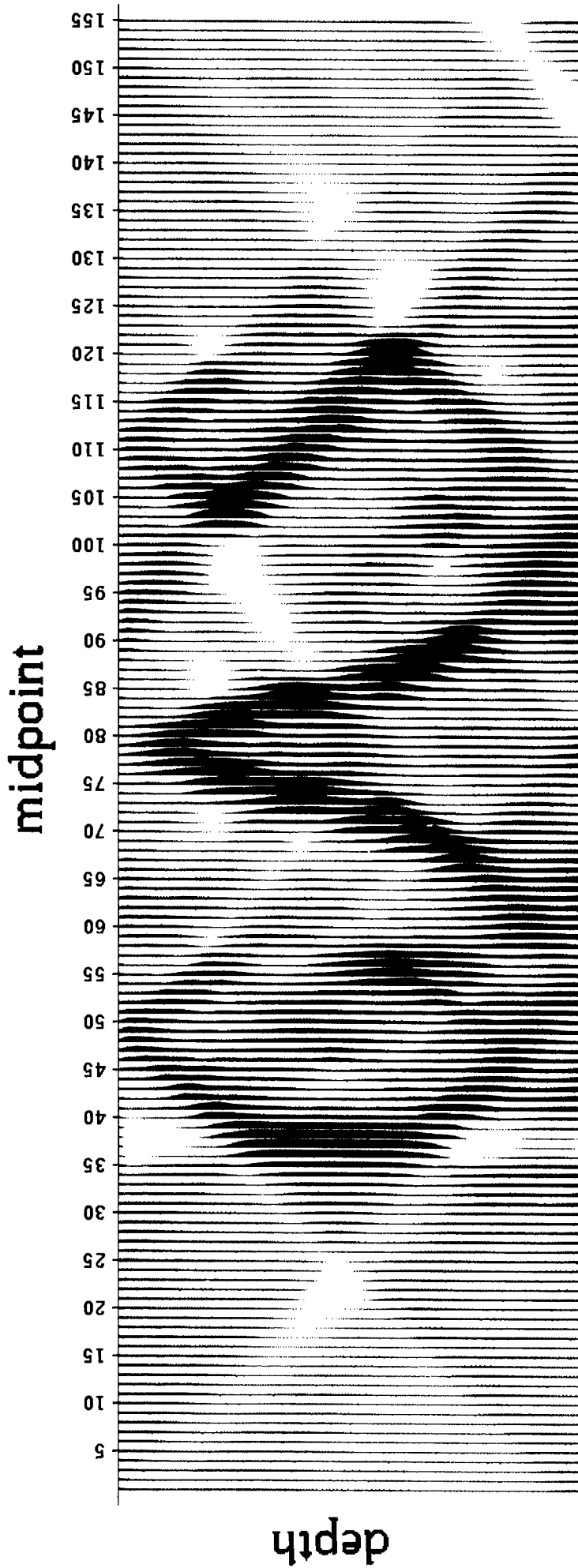
FIG. 7.13. Result of applying the wavenumber-domain inversion to the synthetic in figure 7.11. The interval from the reflector was divided into 48 layers. Note that the components of the original model with dips outside the range of dips used in the calculation of the model have been lost.
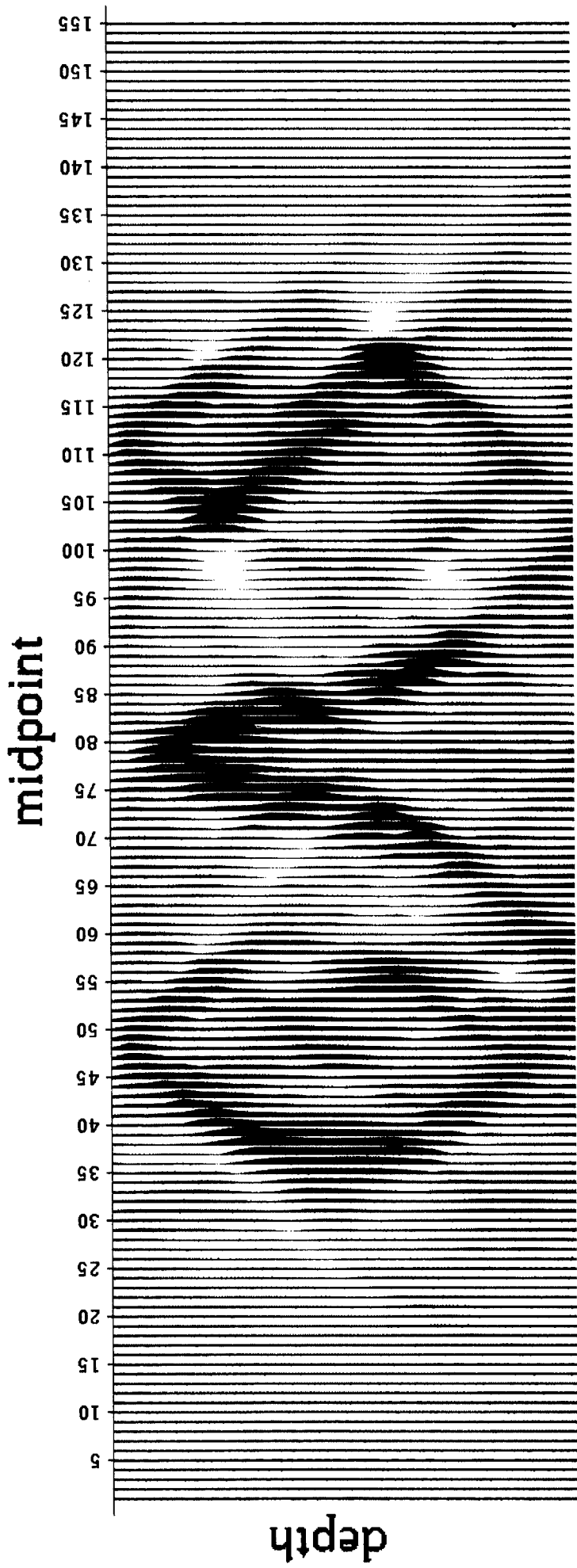
FIG. 7.14. Result of applying the iterative-median inversion to the synthetic in figure 7.11.

the ends of the data on figure 7.13 are absent on figure 7.14. The combined effect of the model calculation and the inversion is in both cases to filter out dips that are outside the range of dips for the rays that sampled the model.

Inversion of Field Data

We applied the MI inversion to the amplitude data in figure 7.7, as well as to the traveltime data. The application of the inversion to the amplitude data rests on two assumptions, that the amplitude fluctuations are caused by absorption, and that the waves are sufficiently band-limited so that equation (7.2) is applicable. Since the data were not deconvolved, it is to be expected that the combined effects of water bottom multiples and shot waveform would result in a highly peaked spectrum and amplitude decay similar to that of a monochromatic wave. This assumption could be made more appropriate by using only the power in a narrow spectral window. Besides absorption, the most likely candidates for the cause of the amplitude fluctuations are scattering and focusing effects caused by lateral variations in velocity. It is difficult to see how scattering could account for amplitude changes by a factor of three, at frequencies as low as 25 Hz. All the reflectors above the bright spot are weak in comparison to the bright spot; consequently all of the transmission coefficients should be close to unity. Focusing from small scale velocity structures can easily result in large amplitude variations. As a working hypothesis we are assuming that the effects of raybending on amplitudes may be neglected. The validity of this assumption remains to be tested.

Figure 7.15 shows the result of the inversion of the amplitude data. The most noteworthy feature of this display is the band of alternating peaks and lows that start near the surface around midpoint 100, reach a depth of about one-quarter the depth to the reflector around midpoint 200, and get gradually shallower toward the right side of the section. Inspection of figure 7.6 shows a series of diffractions at corresponding locations. These diffractions are much less noticeable on the conventional stacked section than on the unstacked data. Since the field data does not carry information about components of the earth model that dip less than the rays at maximum offset, the long wavelength components of the velocity structure are not shown.

We are unable to conclude anything about magnitude of attenuation; only changes over distances less than a cable length are indicated. One constraint that must be satisfied, however, is that the attenuation be non-negative. From laboratory data [Winkler and Nur, 1979], it is known that attenuation is very sensitive to small changes in the state of the rocks and the pore fluids, and can easily change to several times its minimum value.

Figure 7.16 shows the result of applying the inversion to the traveltime data shown in figure 7.9. The noise level is considerably greater than in the amplitude inversion, but the same general features are shown. A clear correlation between peaks in slowness and low attenuation values is evident from the inversions. This is somewhat surprising since higher velocities tend to be associated with lower attenuation in rocks under most, but not all conditions. Laboratory results [Winkler and Nur, 1979; Winkler, 1979; Frisillo and Stewart, 1979] show that attenuation first increases, reaches a peak, and then decreases as gas or air is introduced into a liquid-saturated rock, while P-wave velocity drops with increasing gas saturation. If focusing effects have significant effects on the amplitude anomalies, the tendency would be for the rays that cross through high-velocity lenses to diverge. Further work is needed to determine to what extent this can explain the observed amplitude anomalies.

The main exception from this correlation is the large shallow anomaly around midpoint 110, that shows both time delays and low amplitudes for rays crossing it. This is as would be expected on the basis of the laboratory data if this region contained a diffuse pocket of gas, perhaps connected by faults with the producing gas reservoir that gives rise to the bright-spot reflection.

We have not calibrated the output of the inversions. Most of the observed features appear to be localized and have dimensions that are similar to the spatial resolution of the data. This is in part because the low dip components of the anomalies have been lost. The observed variations in traveltimes are actually quite small - about 10 milliseconds out of a total traveltime of more than 2 seconds, thus a 5% change in velocity over one-tenth of the path could account for the observed effects. A typical amplitude anomaly may be about a factor of 3 in amplitude at 25 Hz; this implies an average

differential Q of about 150 for the whole path or 15 if the attenuation takes place over one-tenth of the path.

Conclusions

The results of this study show that a substantial amount of information is carried in the unstacked seismic data, in both the amplitudes and travel-times of events. The amplitudes carry information about both velocity and intrinsic absorption; the relative importance of the two contributions is still uncertain. Several different techniques are available to analyze this information: we have demonstrated that a relatively simplistic approach can give valuable results when applied to high-quality seismic data. There are a number of ways to improve on some of the assumptions that we have made, and this should result in a corresponding improvement of the results. The velocity and attenuation information thus obtained should be useful, both in the geologic interpretation of the prospects and to improve the stacking and migration of the data.